



# Transmission, refraction and dark-field retrieval in hard X-ray grating interferometry

Zhili Wang,<sup>a\*</sup> Xiaomin Shi,<sup>a</sup> Kun Ren,<sup>a</sup> Heng Chen,<sup>a</sup> Yuqi Ren,<sup>b</sup> Kun Gao<sup>c</sup> and Zhao Wu<sup>c</sup>

<sup>a</sup>School of Electronic Science and Applied Physics, Hefei University of Technology, Anhui 230009, People's Republic of China, <sup>b</sup>Shanghai Synchrotron Radiation Facility, Shanghai Institute of Applied Physics, Chinese Academy of Sciences, Shanghai 201204, People's Republic of China, and <sup>c</sup>National Synchrotron Radiation Laboratory, University of Science and Technology of China, Anhui 230026, People's Republic of China. \*Correspondence e-mail: dywangzl@hfut.edu.cn

Received 6 April 2019

Accepted 25 December 2019

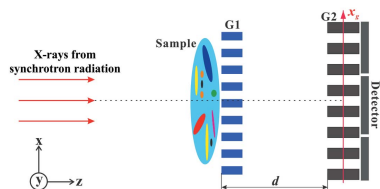
Edited by A. Momose, Tohoku University, Japan

**Keywords:** X-ray imaging; phase-contrast; grating interferometry; three-image algorithm.

A three-image algorithm is proposed to retrieve the sample's transmission, refraction and dark-field information in hard X-ray grating interferometry. Analytical formulae of the three-image algorithm are theoretically derived and presented, and evaluated by proof-of-principle synchrotron radiation experiments. The results confirm the feasibility of the proposed algorithm. The novelty of the proposed algorithm is that it allows versatile and tunable multimodal X-ray imaging by substantially relaxing the existing limitations on the lateral grating position. Furthermore, this algorithm can also be adapted for samples with negligible refraction, reducing the number of required sample measurements to two. Furthermore, the noise properties of the retrieved images are investigated in terms of the standard deviations. Theoretical models are presented and verified by synchrotron radiation measurements. It is shown that the noise standard deviations exhibit strong dependence on the lateral grating position, especially in the case of refraction and dark-field images. Further noise reduction and dose reduction can thus be possible by optimizing the lateral grating position for a selected region of interest. Those results can serve as general guidelines to optimize the data acquisition scheme for specific applications and problems.

## 1. Introduction

Over the last two decades, X-ray phase-contrast imaging has been demonstrated to provide improved contrast for objects made of low-atomic-number elements, such as biological soft tissues with limited attenuation differences (Bravin *et al.*, 2013; Wilkins *et al.*, 2014). Among various X-ray phase-contrast imaging methods, X-ray grating interferometry (XGI) is a promising method to complement conventional X-ray attenuation-contrast imaging, and has its unique advantages: it is compatible with incoherent sources (Pfeiffer *et al.*, 2006a), has a spatial resolution of the order of tens of micrometres, and offers high phase sensitivity (Birnbacher *et al.*, 2016). Furthermore, the sample's transmission, refraction (*i.e.* differential phase-shift) and dark-field signals are measured from a single data set in XGI (Pfeiffer *et al.*, 2008). While the refraction signal is exploited to provide superior soft-tissue contrast, the dark-field signal enables the detection of features with a scale below the spatial resolution of the imaging system (Yashiro *et al.*, 2010). These three different modalities deliver valuable complementary information for better identification and discrimination between materials and types of tissues. In recent years, a variety of potential applications of hard X-ray grating interferometry have been explored, including, but not limited to, dynamic biomedical imaging (Hoshino *et al.*, 2014),



enhanced sensitivity and specificity in mammography (Grandl *et al.*, 2015), materials science (Ruiz-Yaniz *et al.*, 2016), non-destructive testing (Ruiz-Yaniz *et al.*, 2015; Bachche *et al.*, 2017), wavefront metrology (Kayser *et al.*, 2017) and detection of early lung injury (Hellbach *et al.*, 2018; Gradl *et al.*, 2019).

In XGI, the sample's transmission, refraction and dark-field signals are entangled in the acquired projection images. Therefore, several approaches have been developed for quantitative information retrieval from intensity measurements (Momose *et al.*, 2003, 2009; Weitkamp *et al.*, 2005; Modregger *et al.*, 2012; Pelliccia *et al.*, 2013; Wang *et al.*, 2013; Bevins *et al.*, 2012; Ge *et al.*, 2014; Wang *et al.*, 2014; Li *et al.*, 2016; Marschner *et al.*, 2016; Zdora *et al.*, 2017), which is prerequisite for subsequent quantitative analysis and processing, and image interpretation. The phase stepping (PS) technique has been used as the standard approach for signal extraction (Momose *et al.*, 2003; Weitkamp *et al.*, 2005). In this technique, one of the gratings is stepped laterally by a fraction of its period whereby the image acquisition is performed for at least three grating positions. Typically, these grating positions are equally spaced within one grating period. As an alternative, a three-image algorithm is presented to extract transmission, refraction and scattering information for hard X-ray grating interferometry (Pelliccia *et al.*, 2013). However, this algorithm has the inherent restriction that the sample scan must be exactly in phase with the reference scan, and its accuracy is lost in the case of large refraction and/or dark-field signals (Rigon *et al.*, 2007). Recently, angular signal radiography (ASR) was proposed to extract the specimen's absorption, refraction and scattering properties (Li *et al.*, 2016). This approach requires acquisition of multiple images at those so-called valley, up-slope, peak and down-slope positions.

So far, the above approaches for information retrieval share the common restriction that multiple images are acquired at predetermined grating positions. However, it has already been observed that there are indeed some preferential positions for the three different signals. For a given refraction signal, the maximum intensity change occurs at grating positions where the slope of the transmission function is at maximum (Li *et al.*, 2016), while for the dark-field signal the maximum change in intensity is observed at grating positions where the second-order derivative of the transmission function is maximized (Pelliccia *et al.*, 2013). Therefore, there remains an opportunity to explore the potential of a tunable lateral grating position for optimized data acquisition and information retrieval in XGI.

In this work, we present a novel three-image algorithm to retrieve the sample's transmission, refraction and dark-field signals quantitatively in XGI. This technique was inspired by similar approaches for edge illumination (Endrizzi *et al.*, 2014) and recently for analyzer-based imaging (Wang *et al.*, 2018). Analytical formulae for information retrieval are theoretically derived and presented, and validated by proof-of-principle synchrotron radiation experiments. The novelty of the three-image algorithm is that it relaxes the restrictions put on the lateral grating position, which therefore allows versatile and

tunable multimodal X-ray imaging for specific demands. The algorithm can be further simplified for samples with negligible refraction, where only two sample images are sufficient to extract transmission and dark-field signals. Finally, the noise properties of the retrieved images are investigated in terms of the standard deviations. The obtained theoretical models are confirmed by synchrotron radiation measurements.

## 2. Three-image algorithm for information retrieval

As schematically shown in Fig. 1, the typical XGI setup using synchrotron radiation mainly comprises two gratings and a detector. A first phase grating G1 is utilized to generate a periodic interference pattern at specific distances downstream. A sample placed just before G1 will cause local distortions in the interference pattern. The period of the interference pattern, of the order of a few micrometres, is usually much smaller than the pixel size of conventional detectors, of the order of several tens of micrometres. Therefore, a second absorption grating G2, with the same periodicity as that of the interference pattern, is used to convert those local pattern distortions into intensity variations recorded by the detector. In the case of laboratory X-ray sources, a third absorption grating is introduced to split the large focal spot into an array of line sources, each meeting the spatial coherence requirement of the fractional Talbot effect (Wang *et al.*, 2010). The period of the source grating is chosen such that the intensity patterns created by each virtual line source overlap constructively in the detector plane.

With the sample placed immediately before G1, the intensity oscillation  $I(x_g)$  measured by each detector pixel can be written as (Pfeiffer *et al.*, 2008)

$$I(x_g) = I_0 \left[ 1 + V \cos \left( \frac{2\pi x_g}{p_2} + \phi \right) \right], \quad (1)$$

where  $I_0$ ,  $V$  and  $\phi$  are the mean intensity, the visibility and the phase of the intensity oscillation, respectively,  $x_g$  is the lateral position of G2 with respect to the interference pattern, and  $p_2$  is the grating period. For notation brevity, the spatial dependence of all terms has been omitted in equation (1).

For quantitative transmission, refraction and dark-field retrieval, one needs to compare the sample measurement with a sample in the field of view, with the reference measurement without sample, and thereby deduce the local changes in the

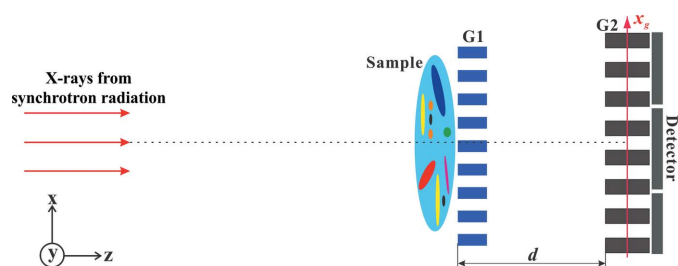


Figure 1 Schematic setup of hard X-ray grating interferometry using synchrotron radiation.

beam propagation due to the sample. In the following, the superscripts ‘s’ and ‘r’ will be consistently used to refer to the sample and reference measurements, respectively. The transmission signal  $T$  is given by the ratio of the mean intensity with sample  $I_0^s$  and without sample  $I_0^r$ ,

$$T = I_0^s / I_0^r = \exp[-\int \mu(x, y, z) dz], \quad (2)$$

where  $\mu(x, y, z)$  is the sample’s linear attenuation coefficient. The refraction signal  $\theta_R$  can be retrieved from the difference of the sample phase  $\phi^s$  and the reference phase  $\phi^r$ ,

$$\theta_R = \frac{p_2}{2\pi d} (\phi^s - \phi^r), \quad (3)$$

where  $d$  is the distance between G1 and G2. The dark-field signal  $D$  is given by the local decrease of the visibility of the intensity oscillation,

$$D = V^s / V^r \quad (4)$$

These three signals are displayed in the form of images.

Let us consider three images acquired with the lateral grating positions set to  $x_g^1 = -x_g^3 = \Delta x$  and  $x_g^2 = 0$ , respectively. By use of equation (1), the following system can be written

$$I_i = I_0 \left[ 1 + V \cos\left(\phi + \frac{2\pi x_g^i}{p_2}\right) \right] \quad (i = 1, 2, 3) \quad (5)$$

that can be analytically solved for  $I_0$ ,  $\phi$  and  $V$ ,

$$\begin{aligned} I_0 &= \frac{I_1 + I_3 - 2I_2 \cos(2\pi\Delta x/p_2)}{4\sin^2(\pi\Delta x/p_2)}, \\ \phi &= \arctan\left[\frac{I_1 - I_3}{I_1 + I_3 - 2I_2} \tan\left(\frac{\pi\Delta x}{p_2}\right)\right], \\ V &= \frac{[(I_1 - I_3)^2 \tan^2(\pi\Delta x/p_2) + (I_1 + I_3 - 2I_2)^2]^{1/2}}{I_1 + I_3 - 2I_2 \cos(2\pi\Delta x/p_2)}. \end{aligned} \quad (6)$$

A detailed derivation of equation (6) can be found in Appendix A. It can be readily proved that equation (6) reduces to the three-step PS with  $\Delta x = -p_2/3$ , and the ASR algorithm (Li *et al.*, 2016) with  $\Delta x = -p_2/4$ , respectively.

Note that equation (6) is the main contribution of this work. It represents a novel three-image algorithm for extracting the sample’s transmission, refraction and dark-field images on a pixel-by-pixel basis. A non-uniform reference phase distribution is allowed by the three-image algorithm. More importantly, the form of equation (6) relates to the unique ability of achieving minimum noise level by optimizing the lateral grating position  $\Delta x$  for a region of interest (ROI) in the retrieved images. This property potentially gives an advantage over existing information retrieval techniques for samples which may contain a range of different features of interest and possibly reduces the dose deposition.

Alternatively, the three images can be acquired with the lateral grating positions set to  $x_g^1 = -x_g^3 = \Delta x$  and  $x_g^2 = p_2/2$ , respectively. Following a similar derivation of equation (6), one can yield the analytical solutions for  $I_0$ ,  $\phi$  and  $V$ , respectively,

$$\begin{aligned} I_0 &= \frac{I_1 + I_3 + 2I_2 \cos(2\pi\Delta x/p_2)}{4 \cos^2(\pi\Delta x/p_2)}, \\ \phi &= \arctan\left[\frac{I_3 - I_1}{I_1 + I_3 - 2I_2} \cot\left(\frac{\pi\Delta x}{p_2}\right)\right], \\ V &= \frac{[(I_1 - I_3)^2 \cot^2(\pi\Delta x/p_2) + (I_1 + I_3 - 2I_2)^2]^{1/2}}{I_1 + I_3 + 2I_2 \cos(2\pi\Delta x/p_2)}. \end{aligned} \quad (7)$$

Moreover, we show that the algorithm given by equation (6) can be further simplified for samples with negligible refraction. In this case, only two sample images are sufficient to retrieve the mean intensity  $I_0^s$  and the visibility  $V^s$  by

$$\begin{aligned} I_0^s &= \frac{I_1^s \cos(\phi^r) - I_2^s \cos(2\pi\Delta x/p_2 + \phi^r)}{\cos(\phi^r) - \cos(2\pi\Delta x/p_2 + \phi^r)}, \\ V^s &= \frac{I_1^s - I_2^s}{I_2^s \cos(2\pi\Delta x/p_2 + \phi^r) - I_1^s \cos(\phi^r)}, \end{aligned} \quad (8)$$

while  $I_0^r$ ,  $V^r$  and  $\phi^r$  can be retrieved by equation (6) with three reference images, since there are no dose constraints in the case of reference measurements. A detailed derivation of equation (8) can be found in Appendix B. In the special case of  $\phi^r = 0$  and  $\Delta x = -p_2/2$ , *i.e.* the minimum position of the intensity oscillation, equation (8) reduces to

$$\begin{aligned} I_0^s &= (I_1^s + I_2^s)/2, \\ V^s &= (I_2^s - I_1^s)/(I_1^s + I_2^s), \end{aligned} \quad (9)$$

which reproduces the two-shot approach by Marschner *et al.* (2016).

### 3. Experimental validation

The novelty of the proposed three-image algorithm lies in its ability to utilize three intensity measurements acquired at flexibly chosen grating positions, for quantitative retrieval of the sample’s transmission, refraction and dark-field images. In order to test its validity, synchrotron radiation experiments were performed at beamline BL13W1 of Shanghai Synchrotron Radiation Facility (SSRF) (Xi *et al.*, 2012). The Talbot interferometer consisted of a phase grating G1 that had a pitch of 2.39  $\mu\text{m}$  and introduced a phase shift of  $\pi/2$  at the design energy of 20 keV, and an absorption grating G2 with a pitch of 2.4  $\mu\text{m}$  and made of gold. The inter-grating distance was set to 46.4 mm, *i.e.* the first fractional Talbot distance. The visibility had a value of 52% in the experiments. Images were acquired with a scientific complementary metal-oxide-semiconductor (sCMOS) detector (Hamamatsu ORCA-Flash 4.0V2) with an effective pixel size of 13  $\mu\text{m}$ . For a quantitative evaluation, a 21-step phase-stepping measurement was also performed, and the retrieved images served as ground truth. The exposure time was 6 ms for each image. Note that the validity of equation (1) is absolutely key to the three-image algorithm. Therefore, the measured intensity oscillation in a certain detector pixel is shown in Fig. 2(a), along with the first-order fitting. Note that the first-order fitting was quantitatively in excellent agreement with the measured oscillation, supported by the fact that the calculated correlation coefficient had a

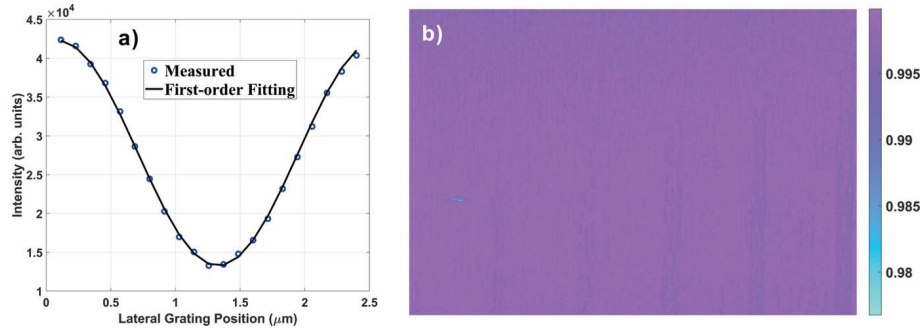


**Figure 2** (a) Measured intensity oscillation as a function of the lateral grating position, along with the first-order fitting in equation (1). (b) Map of the calculated correlation coefficient between the measured intensity oscillation and its first-order fitting over the whole field of view.

value greater than 0.999. Furthermore, the first-order fitting to the measured intensity oscillation was performed across the whole field of view of  $340 \times 500$  pixels. The resulting map of the calculated correlation coefficient is presented in Fig. 2(b). Over the field of view, the correlation coefficient had a mean value of 0.9983. This fact again confirmed the validity of equation (1).

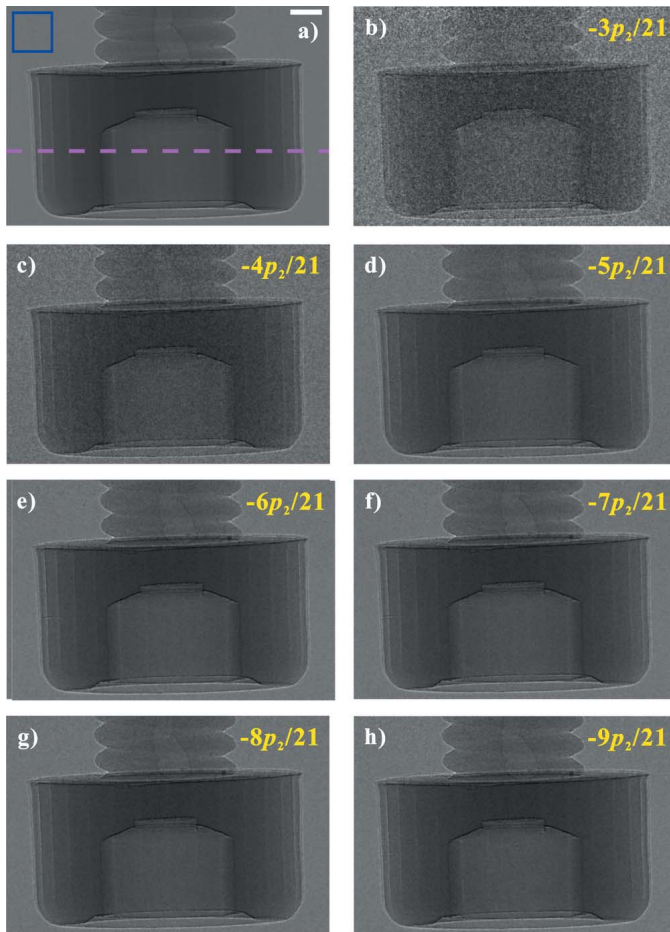


**Figure 3** (a) Transmission image obtained with 21-step PS. (b)–(h) Transmission images obtained with the three-image algorithm, with the corresponding lateral grating position indicated in the panels. Scale bar: 0.65 mm.

Fig. 3 shows the transmission images of a plastic screw. While panel (a) shows the result obtained by 21-step PS, panels (b)–(h) show the images retrieved by the three-image algorithm, with the corresponding lateral grating position indicated. Visually speaking, the qualitative agreement of those images produced by the two techniques is good, despite the increased noise at some positions. For a quantitative comparison, the line profiles along the dashed line marked in panel (a) are displayed in Figs. 4(a)–4(g). The calculated correlation coefficient of the two line profiles is indicated by  $R$  in the corresponding panels. As shown, except for the first two positions, the correlation coefficient has a value greater than 0.977, confirming the feasibility of the proposed three-image algorithm. A few smaller additional peaks are also observed in the line profile plots. This is due to edge enhancement effects occurring upon free-space propagation (Wilkins *et al.*, 1996).

Furthermore, the correlation coefficient only has a value of 0.786 with  $\Delta x = -3p_2/21$ , and 0.924 with  $\Delta x = -4p_2/21$ . Those values are consistent with the increased pixelwise fluctuations observed in Figs. 3(a) and 3(b). For a quantitative explanation, we calculated the standard deviation of the retrieved transmission image by using equations (2) and (6), and error propagation formula (Revol *et al.*, 2010). As the dominant contribution, the noise from photon statistics is considered. The standard deviation  $\sigma_T$  is given by

$$\sigma_T = \left(\sqrt{I_0^r}\right)^{-1} (f^r T^2 A^r + f^s T A^s)^{1/2} \quad (10)$$

with

$$A^{r/s} = \frac{1 + 2\cos^2(2\pi\Delta x^{r/s}/p_2)}{8\sin^4(\pi\Delta x^{r/s}/p_2)} + \left\{ V^{r/s} \cos(\phi^{r/s}) \times \frac{\cos(2\pi\Delta x^{r/s}/p_2)[1 + 2\cos(2\pi\Delta x^{r/s}/p_2)]}{8\sin^4(\pi\Delta x^{r/s}/p_2)} \right\},$$

where the coefficients  $f^{r/s}$  are linked to the detector's transfer properties. As revealed by equation (10),  $\sigma_T$  is inversely proportional to the square root of the mean intensity  $I_0^r$ , and dependent on the sample's transmission  $T$ . Furthermore,  $\sigma_T$

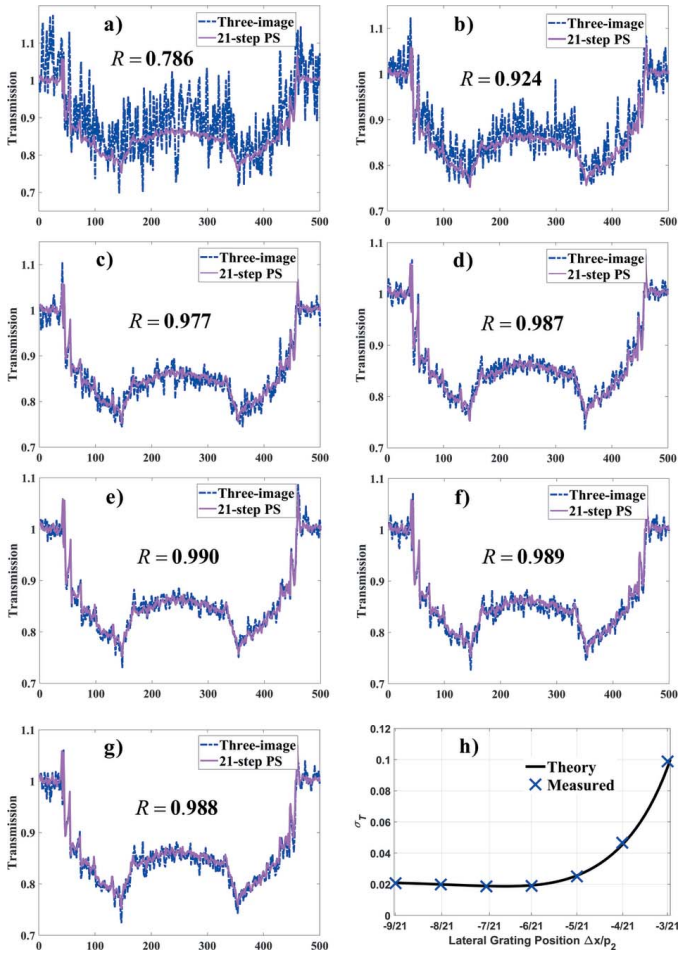


**Figure 4** (a)–(g) Line profiles along the dashed line indicated in Fig. 3(a), together with the calculated correlation coefficient  $R$ . (h) Experimentally measured (crosses) and theoretically predicted (solid line) values of  $\sigma_T$  as a function of the lateral grating position.

has dependence on the lateral grating positions  $\Delta x^{r/s}$ , the visibilities  $V^{r/s}$  and the phases  $\phi^{r/s}$ . In the special case of  $\Delta x^{r/s} = -p_2/3$ ,  $\sigma_T$  is independent of the quantities  $V^{r/s}$  and  $\phi^{r/s}$ . This corresponds to the case of three-step PS, and the final expression is in agreement with those published (Revol *et al.*, 2010; Weber *et al.*, 2011).

To confirm equation (10), the standard deviation  $\sigma_T$  was extracted from a background region of  $50 \times 50$  pixels marked by a square in Fig. 3(a). Fig. 4(h) shows the measured  $\sigma_T$  as a function of the lateral grating position, together with theoretical predictions from equation (10). Excellent agreement is achieved between experimentally measured values and those calculated using the theoretical model.

The retrieved refraction images of a plastic screw are displayed in Fig. 5. The result obtained by 21-step PS is shown in panel (a), and panels (b)–(h) show the images retrieved by the three-image algorithm, with the corresponding lateral grating position indicated in the panels. Again, the visual appearance is very similar for those images. For a quantitative evaluation, Figs. 6(a)–6(g) present the line profiles along the dashed line marked in panel (a). A refraction angle up to

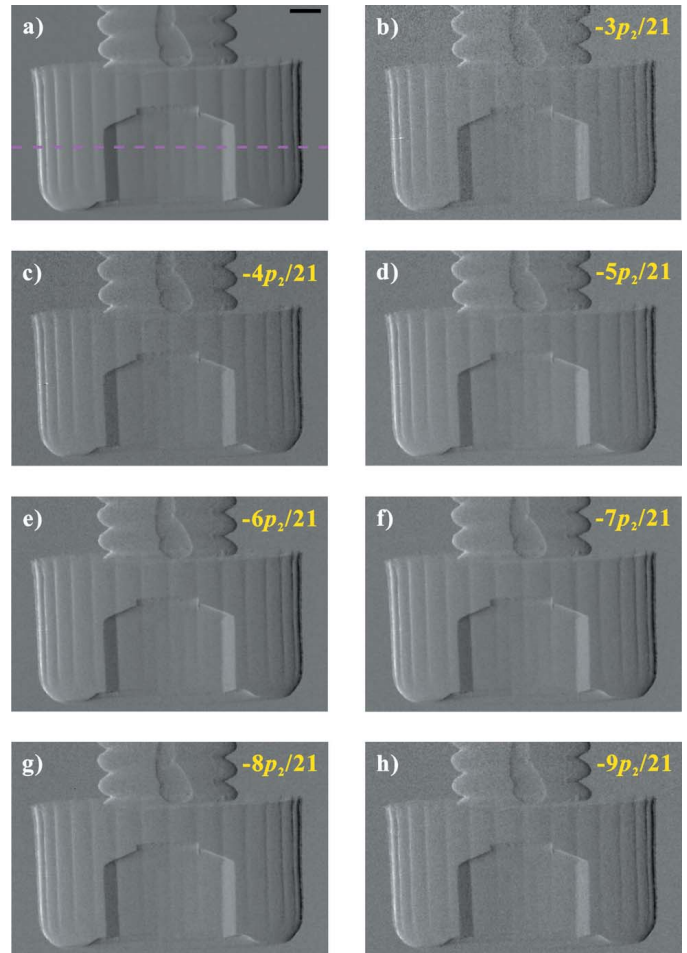


**Figure 5** (a) Refraction image retrieved by 21-step PS. (b)–(h) Refraction images retrieved by the three-image algorithm, with the corresponding lateral grating position indicated in the panels. Scale bar: 0.65 mm.

$9.5 \mu\text{rad}$  is correctly retrieved. This value is comparable with the quantity  $p_2/(4d)$  in our experiment. As shown in Fig. 6, the two line profiles show a good quantitative agreement. The correlation coefficient of the line profiles, indicated by  $R$ , always has a value greater than 0.952. Besides, some local minor differences are also noticeable between the two line profiles. This can be mainly attributed to the fact that only three intensity measurements are used by the three-image algorithm. Despite the small differences, the results obtained with both algorithms are largely consistent, thus confirming the validity of the novel approach.

In addition, the noise behavior of the retrieved refraction image is investigated. Photon statistics noise, as the dominant contribution, is taken into consideration. The standard deviation  $\sigma_{\theta_R}$  of the retrieved refraction image was calculated by use of equation (3) and (6), and error propagation formula (Revol *et al.*, 2010), and given by

$$\sigma_{\theta_R} = \frac{p_2}{2\pi d} \left( \sqrt{I_0^r} \right)^{-1} \left( \frac{f^r B^r}{V^{r^2}} + \frac{f^s B^s}{TV^{s^2}} \right)^{1/2}, \quad (11)$$

with

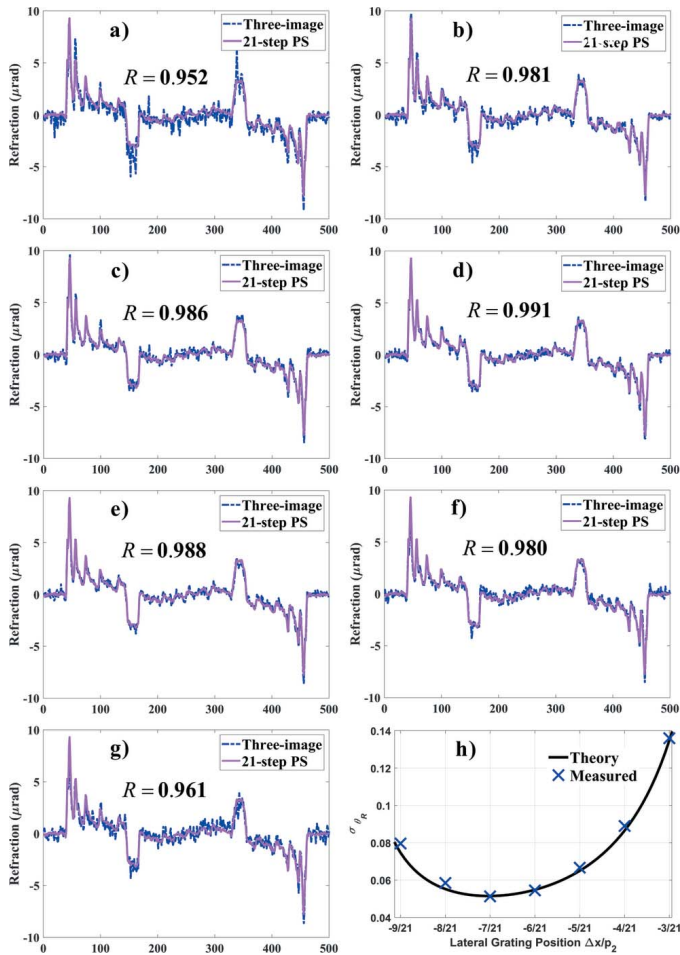


**Figure 6**  
(a)–(g) Line profiles along the dashed line indicated in Fig. 5(a), together with the calculated correlation coefficient  $R$ . (h) Experimentally measured (crosses) and theoretically predicted (solid line) values of  $\sigma_{\theta_R}$  against the lateral grating position.

$$\begin{aligned}
 B^{r/s} = & \frac{\tan^2(\pi\Delta x^{r/s}/p_2)}{16 \sin^6(\pi\Delta x^{r/s}/p_2)} \left\{ 2 + \cos\left(\frac{2\pi\Delta x^{r/s}}{p_2}\right) \right. \\
 & \left. - \cos(2\phi^{r/s}) \left[ 1 + 2 \cos\left(\frac{2\pi\Delta x^{r/s}}{p_2}\right) \right] \right\} \\
 & + \frac{V^{r/s} \tan^2(\pi\Delta x^{r/s}/p_2)}{16 \sin^6(\pi\Delta x^{r/s}/p_2)} \left\{ \frac{\cos(\phi^{r/s})}{2} \right. \\
 & \times \left[ 1 + 2 \cos\left(\frac{2\pi\Delta x^{r/s}}{p_2}\right) \right] \left[ 2 - \cos\left(\frac{2\pi\Delta x^{r/s}}{p_2}\right) \right] \\
 & \left. - \cos(3\phi^{r/s}) \left[ \frac{1}{2} + \cos^2\left(\frac{\pi\Delta x^{r/s}}{p_2}\right) \right] \right\},
 \end{aligned}$$

from which it can be seen that, besides being dependent on the mean intensity  $I_0^r$ ,  $\sigma_{\theta_R}$  is also dependent on the visibilities  $V^{r/s}$ , the sample's transmission  $T$ , and the phases  $\phi^{r/s}$ . The first term of  $B^{r/s}$  has no dependence on the visibilities  $V^{r/s}$ , and can be independent of the phases  $\phi^{r/s}$  in the special case of  $\Delta x^{r/s} = -p_2/3$ . By contrast, the second term of  $B^{r/s}$  is proportional to the visibilities  $V^{r/s}$ , and always has dependence on the phases

$\phi^{r/s}$ . In the special case of  $\Delta x^{r/s} = -p_2/3$ , the resulting expression of  $\sigma_{\theta_R}$  is in agreement with those reported by Wu *et al.* (2015).

To validate equation (11), the standard deviation  $\sigma_{\theta_R}$  was extracted over the same square area marked in Fig. 3(a). As shown in Fig. 6(h), experimentally measured values agree excellently with theoretical predictions. Actually, the expression of equation (11) suggests that, for a given ROI characterized by  $\phi^{r/s}$  and  $V^{r/s}$ , there is always an optimal grating position at which  $\sigma_{\theta_R}$  achieves its minimum. This may result in further possible dose reduction, which can be important for imaging of dose-sensitive samples.

Fig. 7 presents the dark-field images obtained from the same experimental data. A qualitative comparison between panel (a) and panels (b)–(h) indicates that the results of the three-image algorithm are similar to that of 21-step PS. Note the different color scales used. A comparison between Figs. 7 and 5 indicates that the dark-field signal is more sensitive to the reduced photon counts. To test the quantitative accuracy of the three-image algorithm, the normalized mean squared error (NMSE) of panels (b)–(h) and panel (a) was calculated, and the result is shown in Fig. 8(a). Despite the cases of  $-3p_2/21$  and  $-4p_2/21$ , the NMSE only has a value lower than 0.01. Besides, the monotonic increase of NMSE with  $\Delta x/p_2$

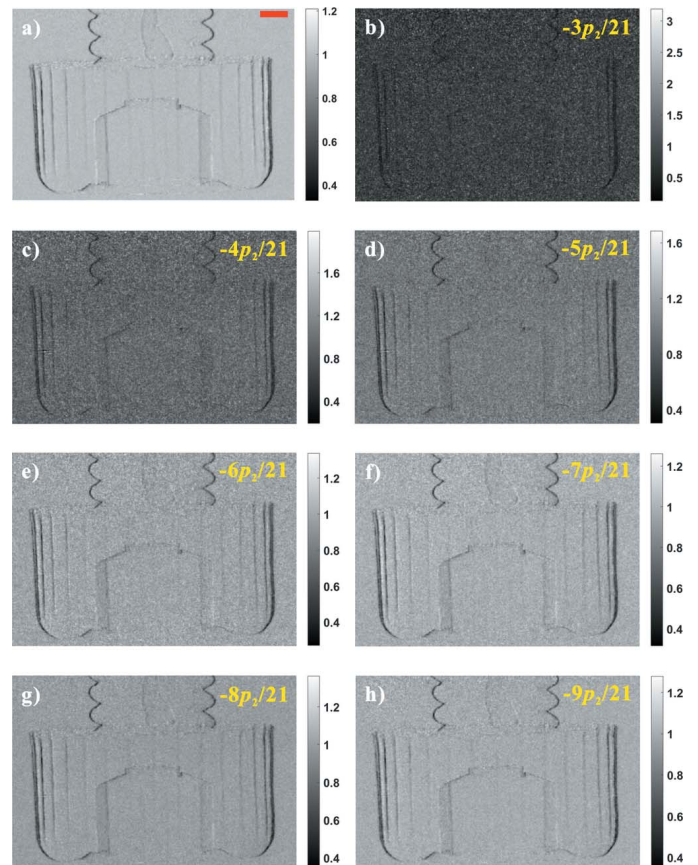


**Figure 7**  
(a) Dark-field image retrieved by 21-step PS. (b)–(h) Dark-field images retrieved by the three-image algorithm, together with the normalized mean square error (NMSE) with respect to (a). Scale bar: 0.65  $\mu\text{m}$ .

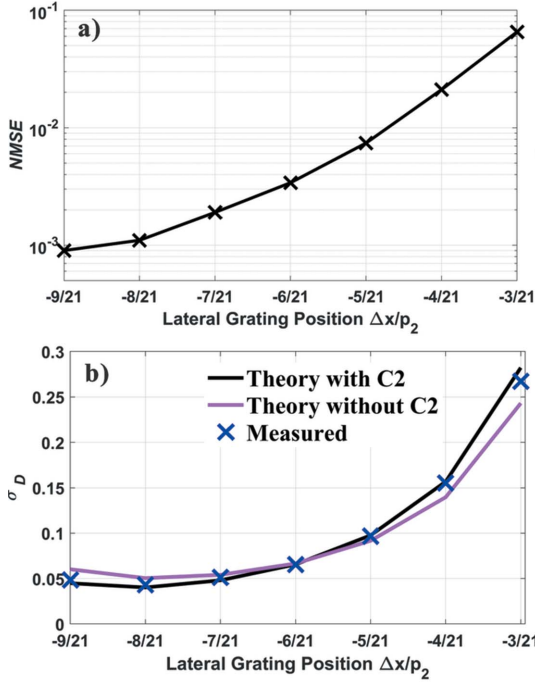


**Figure 8**  
 (a) Logarithm of the normalized mean square error against the lateral grating position. (b) Experimentally measured (crosses) and theoretically predicted (solid line) values of  $\sigma_D$  against the lateral grating position.

indicates that the lateral grating position close to  $-p_2/2$  may be preferred by the dark-field signal. In addition, the standard deviation of the dark-field image was also calculated by use of equations (4) and (6), and error propagation formula (Revol *et al.*, 2010). The resulting expression of the standard deviation  $\sigma_D$  is given by

$$\sigma_D = \left( V^r \sqrt{I_0^r} \right)^{-1} \left( \frac{f^s C^s}{T} + f^r D^2 C^r \right)^{1/2}, \quad (12)$$

with

$$C^{r/s} = \frac{C_1^{r/s}}{16 \sin^4(\pi \Delta x^{r/s} / p_2)} + \frac{V^{r/s} C_2^{r/s}}{16 \sin^4(\pi \Delta x^{r/s} / p_2)},$$

$$\begin{aligned} C_1^{r/s} = & 2(V^{r/s})^2 \left[ 1 + 2 \cos^2 \left( \frac{2\pi \Delta x^{r/s}}{p_2} \right) \right] \\ & + 4V \cos(\phi^{r/s}) \left[ 1 + 2 \cos \left( \frac{2\pi \Delta x^{r/s}}{p_2} \right) \right] \\ & + \left\{ 4 + 2 \cos \left( \frac{2\pi \Delta x^{r/s}}{p_2} \right) \right. \\ & \left. + 2 \cos(2\phi^{r/s}) \left[ 1 + 2 \cos \left( \frac{2\pi \Delta x^{r/s}}{p_2} \right) \right] \right\} \\ & / \left[ 1 + \cos \left( \frac{2\pi \Delta x^{r/s}}{p_2} \right) \right], \end{aligned}$$

$$\begin{aligned} C_2^{r/s} = & 2(V^{r/s})^2 \cos(\phi^{r/s}) \cos \left( \frac{2\pi \Delta x^{r/s}}{p_2} \right) \\ & \times \left[ 1 + 2 \cos \left( \frac{2\pi \Delta x^{r/s}}{p_2} \right) \right] \\ & + 2V^{r/s} \left[ 1 + 2 \cos \left( \frac{2\pi \Delta x^{r/s}}{p_2} \right) \right] [2 + \cos(2\phi^{r/s})] \\ & - 6V^{r/s} + \left\{ \cos(\phi^{r/s}) \left[ 1 + 2 \cos \left( \frac{2\pi \Delta x^{r/s}}{p_2} \right) \right] \right. \\ & \left. \times \left[ 2 + \cos \left( \frac{2\pi \Delta x^{r/s}}{p_2} \right) \right] \right\} / \left[ 2 \cos^2 \left( \frac{\pi \Delta x^{r/s}}{p_2} \right) \right] \\ & + \left\{ \cos(3\phi^{r/s}) \left[ 1 + 2 \cos^2 \left( \frac{\pi \Delta x^{r/s}}{p_2} \right) \right] \right\} \\ & / \left[ 2 \cos^2 \left( \frac{\pi \Delta x^{r/s}}{p_2} \right) \right]. \end{aligned}$$

As shown in equation (12), in addition to the mean intensity  $I_0^r$ ,  $\sigma_D$  is influenced by the visibilities  $V^{r/s}$ , the sample's transmission  $T$  and the phases  $\phi^{r/s}$  through  $C^{r/s}$ . To verify equation (12), the standard deviation  $\sigma_D$  was extracted over the rectangle region marked in Fig. 3(a). As shown in Fig. 8(b), very good agreement is observed between experimentally measured and theoretically predicted values. The optimal grating position at which  $\sigma_D$  achieves its minimum obviously deviates from  $-p_2/3$  used in the three-step PS. This result again indicates the potential of noise reduction by grating position optimization.

We note that under the assumption of low visibility the term  $C_2^{r/s}$  has been reasonably neglected in the literature (Weber *et al.*, 2011). However, this approximation is no longer valid in the case of high visibility. As demonstrated in Fig. 8(b), with a reference visibility of 0.52, the theoretical values of  $\sigma_D$  without  $C_2^{r/s}$  exhibit obvious deviations from experimental measurements. In the worst case of  $-9p_2/21$ , the relative error can be greater than 30%. Those results emphasize the importance of equation (12) for a comprehensive understanding of the noise behavior of the dark-field image.

Finally, we would like to point out that equations (10)–(12) emphasize the unique potential of the novel three-image algorithm for noise suppression of versatile ROIs in the retrieved images. In order to determine the optimal lateral grating position, both the reference parameters  $I_0^r$ ,  $\phi^r$  and  $V^r$  and the sample parameters  $I_0^s$ ,  $\phi^s$  and  $V^s$  (*i.e.*  $T$ ,  $\theta_R$  and  $D$ ) have to be taken into consideration. On the one hand, the reference parameters can be measured experimentally, either by our three-image algorithm or by a phase-stepping procedure. On the other hand, the sample parameters cannot be known before imaging generally. Alternatively, the knowledge from other techniques or tissue-mimicking materials can be used to provide an initial guess of  $T$ ,  $\theta_R$  and  $D$ . With these parameters known, one can draw a contour map showing the noise standard deviation as a functions of  $\Delta x^r$  and  $\Delta x^s$ . Then the optimized grating positions can be identified by the minimum of the standard deviation. Note that the above

procedure is applicable on a pixel-by-pixel basis. For a ROI, the properly weighed values of the reference and sample parameters over the region should be used to determine the optimal lateral grating positions.

#### 4. Conclusion

A novel three-image algorithm is proposed for quantitative retrieval of transmission, refraction and dark-field signals in hard X-ray grating interferometry. Analytical formulae are theoretically derived and presented for simultaneous information retrieval. The validity of the proposed three-image algorithm is essentially based on the first-order approximation of the intensity oscillation, and confirmed by results from proof-of-principle synchrotron radiation experiments. The main strength of the algorithm with respect to existing algorithms is that it relaxes restrictions on the lateral grating position, and therefore allows flexible and tunable multimodal X-ray imaging. Moreover, the retrieval formula can be further simplified for samples featuring negligible refraction, potentially reducing the number of required sample images to two. Finally, the presented formalism can be straightforwardly extended to neutron grating interferometry (Pfeiffer *et al.*, 2006b).

More importantly, the noise behavior, in terms of the standard deviation, of the retrieved images is theoretically investigated. The obtained theoretical models are verified by synchrotron radiation measurements. As shown, the standard deviations are strongly dependent on the lateral grating positions, particularly in the case of refraction and dark-field images. These results emphasize the potential of noise reduction and possible reduction in dose deposition by grating position optimization for a selected ROI. Besides, it is noted that special care has to be taken when dealing with the standard deviation of the dark-field image, since the previously neglected term can have a substantial contribution in some cases. Those results can be used as general guidelines to optimize the data acquisition procedure for specific applications and demands, and provide a comprehensive understanding of the noise characteristics of hard X-ray grating interferometry. Future work will be devoted to a fair comparison between the three-image algorithm and the phase-stepping technique.

#### APPENDIX A

##### Detailed derivation of equation (6)

According to equation (1), the measured intensities of the three projection images are given by

$$\begin{aligned} I_1 &= I_0 \left[ 1 + V \cos \left( \phi + \frac{2\pi\Delta x}{p_2} \right) \right], \\ I_2 &= I_0 [1 + V \cos(\phi)], \\ I_3 &= I_0 \left[ 1 + V \cos \left( \phi - \frac{2\pi\Delta x}{p_2} \right) \right]. \end{aligned} \quad (13)$$

##### A1. The mean intensity $I_0$

Based on equation (13), one has

$$\begin{aligned} I_1 + I_3 - 2I_2 \cos \left( \frac{2\pi\Delta x}{p_2} \right) &= 2I_0 \left[ 1 - \cos \left( \frac{2\pi\Delta x}{p_2} \right) \right] \\ &= 4I_0 \sin^2 \left( \frac{\pi\Delta x}{p_2} \right), \end{aligned} \quad (14)$$

from which the mean intensity  $I_0$  can be retrieved,

$$I_0 = \frac{I_1 + I_3 - 2I_2 \cos(2\pi\Delta x/p_2)}{4 \sin^2(\pi\Delta x/p_2)}. \quad (15)$$

##### A2. The phase $\phi$

Based on equation (13), one yields

$$\begin{aligned} I_1 - I_3 &= -2I_0 V \sin \left( \frac{2\pi\Delta x}{p_2} \right) \sin(\phi) \\ &= -4I_0 V \sin \left( \frac{\pi\Delta x}{p_2} \right) \cos \left( \frac{\pi\Delta x}{p_2} \right) \sin(\phi), \\ I_1 + I_3 - 2I_2 &= 2I_0 V \left[ \cos \left( \frac{2\pi\Delta x}{p_2} \right) - 1 \right] \cos(\phi) \\ &= -4I_0 V \sin^2 \left( \frac{\pi\Delta x}{p_2} \right) \cos(\phi), \end{aligned} \quad (16)$$

which results in

$$\frac{I_1 - I_3}{I_1 + I_3 - 2I_2} = \frac{\tan(\phi)}{\tan(\pi\Delta x/p_2)}, \quad (17)$$

and then the phase  $\phi$  can be retrieved,

$$\phi = \arctan \left[ \frac{I_1 - I_3}{I_1 + I_3 - 2I_2} \tan \left( \frac{\pi\Delta x}{p_2} \right) \right]. \quad (18)$$

##### A3. The visibility $V$

Based on equation (13), one obtains

$$\begin{aligned} (I_1 - I_3) \tan \left( \frac{\pi\Delta x}{p_2} \right) &= -4I_0 V \sin^2 \left( \frac{\pi\Delta x}{p_2} \right) \sin(\phi), \\ I_1 + I_3 - 2I_2 &= -4I_0 V \sin^2 \left( \frac{\pi\Delta x}{p_2} \right) \cos(\phi), \end{aligned} \quad (19)$$

which then leads to

$$\begin{aligned} (I_1 - I_3)^2 \tan^2 \left( \frac{\pi\Delta x}{p_2} \right) + (I_1 + I_3 - 2I_2)^2 \\ = \left[ 4I_0 V \times \sin^2 \left( \frac{\pi\Delta x}{p_2} \right) \right]^2. \end{aligned} \quad (20)$$

On substitution of equation (15) into equation (20), one can retrieve the visibility,

$$V = \frac{\left[ (I_1 - I_3)^2 \tan^2(\pi\Delta x/p_2) + (I_1 + I_3 - 2I_2)^2 \right]^{1/2}}{I_1 + I_3 - 2I_2 \cos(2\pi\Delta x/p_2)}. \quad (21)$$

APPENDIX B

Detailed derivation of equation (8)

According to equation (1), for samples with negligible refraction, the measured intensities of the two sample's images are given by

$$I_1^s = I_0^s \left[ 1 + V^s \cos \left( \phi^r + \frac{2\pi\Delta x}{p_2} \right) \right], \quad (22)$$

$$I_2^s = I_0^s [1 + V^s \cos(\phi^r)].$$

B1. The mean intensity  $I_0^s$

Based on equation (22), one has

$$I_1^s \cos(\phi^r) - I_2^s \cos \left( \frac{2\pi\Delta x}{p_2} + \phi^r \right) = I_0^s \left[ \cos(\phi^r) - \cos \left( \frac{2\pi\Delta x}{p_2} + \phi^r \right) \right], \quad (23)$$

from which the mean intensity  $I_0^s$  can be retrieved,

$$I_0^s = \frac{I_1^s \cos(\phi^r) - I_2^s \cos(2\pi\Delta x/p_2 + \phi^r)}{\cos(\phi^r) - \cos(2\pi\Delta x/p_2 + \phi^r)}. \quad (24)$$

B2. The visibility  $V^s$

Based on equation (22), one yields

$$\frac{I_1^s}{I_2^s} = \frac{1 + V^s \cos[(2\pi\Delta x/p_2) + \phi^r]}{1 + V^s \cos(\phi^r)}, \quad (25)$$

which then allows the retrieval of the visibility  $V^s$ ,

$$V^s = \frac{I_1^s - I_2^s}{I_2^s \cos(2\pi\Delta x/p_2 + \phi^r) - I_1^s \cos(\phi^r)}. \quad (26)$$

Funding information

Funding for this research was provided by: National Natural Science Foundation of China (grant Nos. U1532113, 11475170, 11905041, 11805205).

References

Bachche, S., Nonoguchi, M., Kato, K., Kageyama, M., Koike, T., Kuribayashi, M. & Momose, A. (2017). *Sci. Rep.* **7**, 6711.  
 Bevins, N., Zambelli, J., Li, K., Qi, Z. & Chen, G. (2012). *Med. Phys.* **39**, 424–428.  
 Birnbacher, L., Willner, M., Velroyen, A., Marschner, M., Hipp, A., Meiser, J., Koch, F., Schröter, T., Kunka, D., Mohr, J., Pfeiffer, F. & Herzen, J. (2016). *Sci. Rep.* **6**, 24022.  
 Bravin, A., Coan, P. & Suortti, P. (2013). *Phys. Med. Biol.* **58**, R1–35.  
 Endrizzi, M., Diemoz, P. C., Millard, T. P., Louise Jones, J., Speller, R. D., Robinson, I. K. & Olivo, A. (2014). *Appl. Phys. Lett.* **104**, 024106.  
 Ge, Y., Li, K., Garrett, J. & Chen, G. (2014). *Opt. Express*, **22**, 14246–14252.  
 Gradl, R., Morgan, K. S., Dierolf, M., Jud, C., Hehn, L., Günther, B., Möller, W., Kutschke, D., Yang, L., Stoeger, T., Pfeiffer, D., Gleich, B., Achterhold, K., Schmid, O. & Pfeiffer, F. (2019). *IEEE Trans. Med. Imaging*, **38**, 649–656.

Grandl, S., Scherer, K., Sztrókay-Gaul, A., Birnbacher, L., Willer, K., Chabior, M., Herzen, J., Mayr, D., Auweter, S. D., Pfeiffer, F., Bamberg, F. & Hellerhoff, K. (2015). *Eur. Radiol.* **25**, 3659–3668.  
 Hellbach, K., Meinel, F. G., Conlon, T. M., Willer, K., Yaroshenko, A., Velroyen, A., Braunagel, M., Auweter, S., Reiser, M. F., Eickelberg, O., Pfeiffer, F. & Yildirim, A. Ö. (2018). *Sci. Rep.* **8**, 2096.  
 Hoshino, M., Uesugi, K., Tsukube, T. & Yagi, N. (2014). *J. Synchrotron Rad.* **21**, 1347–1357.  
 Kayser, Y., David, C., Flechsig, U., Krempasky, J., Schlott, V. & Abela, R. (2017). *J. Synchrotron Rad.* **24**, 150–162.  
 Li, P., Zhang, K., Bao, Y., Ren, Y., Ju, Z., Wang, Y., He, Q., Zhu, Z., Huang, W., Yuan, Q. & Zhu, P. (2016). *Opt. Express*, **24**, 5829–5845.  
 Marschner, M., Birnbacher, L., Mechlem, K., Noichl, W., Fehringer, A., Willner, M., Scherer, K., Herzen, J., Noël, P. B. & Pfeiffer, F. (2016). *Opt. Express*, **24**, 27032–27045.  
 Modregger, P., Scattarella, F., Pinzer, B., David, C., Bellotti, R. & Stampanoni, M. (2012). *Phys. Rev. Lett.* **108**, 048101.  
 Momose, A., Kawamoto, S., Koyama, I., Hamaishi, Y., Takai, H. & Suzuki, Y. (2003). *Jpn. J. Appl. Phys.* **42**, L866–L868.  
 Momose, A., Yashiro, W., Maikusa, H. & Takeda, Y. (2009). *Opt. Express*, **17**, 12540–12545.  
 Pelliccia, D., Rigon, L., Arfelli, F., Menk, R. H., Bukreeva, I. & Cedola, A. (2013). *Opt. Express*, **21**, 19401–19411.  
 Pfeiffer, F., Bech, M., Bunk, O., Kraft, P., Eikenberry, E., Brönnimann, C., Grünzweig, C. & David, C. (2008). *Nat. Mater.* **7**, 134–137.  
 Pfeiffer, F., Grünzweig, C., Bunk, O., Frei, G., Lehmann, E. & David, C. (2006b). *Phys. Rev. Lett.* **96**, 215505.  
 Pfeiffer, F., Weitkamp, T., Bunk, O. & David, C. (2006a). *Nat. Phys.* **2**, 258–261.  
 Revol, V., Kottler, C., Kaufmann, R., Straumann, U. & Urban, C. (2010). *Rev. Sci. Instrum.* **81**, 073709.  
 Rigon, L., Arfelli, F. & Menk, R. H. (2007). *Appl. Phys. Lett.* **90**, 114102.  
 Ruiz-Yaniz, M., Koch, F., Zanette, I., Rack, A., Meyer, P., Kunka, D., Hipp, A., Mohr, J. & Pfeiffer, F. (2015). *Appl. Phys. Lett.* **106**, 151105.  
 Ruiz-Yaniz, M., Zanette, I., Sarapata, A., Birnbacher, L., Marschner, M., Chabior, M., Olbinado, M., Pfeiffer, F. & Rack, A. (2016). *J. Synchrotron Rad.* **23**, 1202–1209.  
 Wang, Z., Gao, K., Ge, X., Wu, Z., Chen, H., Wang, S., Zhu, P., Yuan, Q., Huang, W., Zhang, K. & Wu, Z. (2013). *J. Phys. D Appl. Phys.* **46**, 494003.  
 Wang, Z., Gao, K., Wang, D., Wu, Z., Chen, H., Wang, S. & Wu, Z. (2014). *Opt. Lett.* **39**, 877–879.  
 Wang, Z., Liu, D., Zhang, J., Huang, W., Yuan, Q., Gao, K. & Wu, Z. (2018). *J. Synchrotron Rad.* **25**, 1206–1213.  
 Wang, Z., Zhu, P., Huang, W., Yuan, Q., Liu, X., Zhang, K., Hong, Y., Zhang, H., Ge, X., Gao, K. & Wu, Z. (2010). *Anal. Bioanal. Chem.* **397**, 2091–2094.  
 Weber, T., Bartl, P., Bayer, F., Durst, J., Haas, W., Michel, T., Ritter, A. & Anton, G. (2011). *Med. Phys.* **38**, 4133–4140.  
 Weitkamp, T., Diaz, A., David, C., Pfeiffer, F., Stampanoni, M., Cloetens, P. & Ziegler, E. (2005). *Opt. Express*, **13**, 6296–6304.  
 Wilkins, S. W., Gureyev, T. E., Gao, D., Pogany, A. & Stevenson, A. W. (1996). *Nature*, **384**, 335–338.  
 Wilkins, S. W., Nesterets, Y. I., Gureyev, T. E., Mayo, S. C., Pogany, A. & Stevenson, A. W. (2014). *Proc. R. Soc. A*, **372**, 20130021.  
 Wu, Z., Gao, K., Chen, J., Wang, D., Wang, S., Chen, H., Bao, Y., Shao, Q., Wang, Z., Zhang, K., Zhu, P. & Wu, Z. (2015). *Med. Phys.* **42**, 741–749.  
 Xi, Y., Kou, B., Sun, H., Qi, J., Sun, J., Mohr, J., Börner, M., Zhao, J., Xu, L. X., Xiao, T. & Wang, Y. (2012). *J. Synchrotron Rad.* **19**, 821–826.  
 Yashiro, W., Terui, Y., Kawabata, K. & Momose, A. (2010). *Opt. Express*, **18**, 16890–16901.  
 Zdora, M. C., Thibault, P., Zhou, T., Koch, F. J., Romell, J., Sala, S., Last, A., Rau, C. & Zanette, I. (2017). *Phys. Rev. Lett.* **118**, 203903.